Nano Energy 35 (2017) 71–78

Contents lists available at ScienceDirect

Nano Energy

journal homepage: www.elsevier.com/locate/nanoen

Communication

# New-type $K_{0.7}Fe_{0.5}Mn_{0.5}O_2$ cathode with an expanded and stabilized interlayer structure for high-capacity sodium-ion batteries

Xuanpeng Wang[a], Ping Hu[a], Chaojiang Niu[a,*], Jiashen Meng[a], Xiaoming Xu[a], Xiujuan Wei[a], Chunjuan Tang[a,b], Wen Luo[a], Liang Zhou[a], Qinyou An[a], Liqiang Mai[a,c,*]

[a] State Key Laboratory of Advanced Technology for Materials Synthesis and Processing, Wuhan University of Technology, Wuhan 430070, China
[b] Department of Mathematics and Physics, Luoyang Institute of Science and Technology, Luoyang 471023, China
[c] Department of Chemistry, University of California, Berkeley, CA 94720, United States

ARTICLE INFO

*Keywords:*
New-type
Cathode materials
Enlarged and stabilized interlayer structure
High-capacity
Sodium-ion batteries

ABSTRACT

The delivery of cathodes with both high capacity and excellent cycling stability is a great challenge in the development of sodium-ion batteries (SIBs) for energy storage systems. Here, we exploited a novel potassium-ion-intercalated layered iron/manganese-based material ($K_{0.7}Fe_{0.5}Mn_{0.5}O_2$). On the basis of advanced *in situ* and *ex situ* X-ray diffraction analysis, we confirm that $K_{0.7}Fe_{0.5}Mn_{0.5}O_2$ can provide highly reversible layer spacing variations and an ultra-stable skeleton structure during the sodiation/desodiation processes. As a result, $K_{0.7}Fe_{0.5}Mn_{0.5}O_2$ displays superior performance, with both high capacity and superior cycling stability, as a cathode for SIBs. A high discharge capacity of 181 mAh $g^{-1}$ is achieved at 100 mA $g^{-1}$. Remarkably, even when cycled at high rate of 1000 mA $g^{-1}$, 85% of the initial discharge capacity is maintained after 1000 cycles. These results indicate that $K_{0.7}Fe_{0.5}Mn_{0.5}O_2$ is a promising candidate for high-capacity and long-life SIBs. Additionally, this work will provide a unique insight into the development of high-performance cathodes for energy storages.

## 1. Introduction

Sodium-ion batteries (SIBs) have been investigated for grid-scale energy storage systems because of the distinct advantages related to the natural abundance and potentially low cost of sodium resources [1–12]. Because of their environmentally friendly and high theoretical capacities, conventional sodium-ions-intercalated layered metal oxide cathode materials, including cobalt-based materials [13–19], nickel-based materials [20–23], vanadium-based materials [24–27], iron-based materials [28–32], chromium-based materials [33,34], and manganese-based materials [35–38], have been widely studied for SIBs. Among these layered materials, the iron/manganese-based material ($Na_{2/3}Fe_{1/2}Mn_{1/2}O_2$) is considered to be one of most promising candidates because of its high capacity and abundance in the Earth's crust [39–43]. However, the poor long-term cycling performance of $Na_{2/3}Fe_{1/2}Mn_{1/2}O_2$ has been demonstrated to be caused by its structural instability upon insertion/de-insertion of sodium ions [44].

To improve the structural stability of $Na_{2/3}Fe_{1/2}Mn_{1/2}O_2$, nanostructures have been widely constructed in sodium storage systems to inhibit structural collapse during the insertion/de-insertion of sodium ions [6–9]. Many researchers have focused on the development of ternary/multiple materials to extend the cycling stability through the transition-metal doping strategy, while this strategy also cut down the initial discharge capacity [45–50]. Thus, electrodes with both high capacity and excellent cycling stability are strongly desired [44,51]. Therefore, the development of a superior strategy to improve the structural stability of layered SIB cathodes with high capacity has become urgent. Recently, an interesting and novel $K^+$ pre-intercalation approach has been proposed to enhance the structural stability during the charge/discharge process [51–58]. Liu et al. adopted a potassium-containing compound ($K_{0.27}MnO_2$) by intercalating potassium ions into manganese oxide to expand the diffusion channels, leading to an improvement in the energy density and cycling stability for SIBs [52]. In our previous study, we demonstrated that $K_3V_2(PO_4)_3$/C bundled nanowires also exhibited excellent cycling stability for SIBs because of the highly stable framework [53].

Herein, we designed a novel cathode material ($K_{0.7}Fe_{0.5}Mn_{0.5}O_2$) and systematically investigated the sodium storage performance of carbon-coated layered iron/manganese-based nanoparticles intercalated with alkali-metal ions ($K^+$, $Na^+$ and $Li^+$), including $K_{0.7}Fe_{0.5}Mn_{0.5}O_2$, $Na_{0.7}Fe_{0.5}Mn_{0.5}O_2$ and $Li_{0.7}Fe_{0.5}Mn_{0.5}O_2$. On the

* Corresponding author.
*E-mail addresses:* niuchaojiang11@whut.edu.cn (C. Niu), mlq518@whut.edu.cn (L. Mai).

http://dx.doi.org/10.1016/j.nanoen.2017.03.026
Received 8 November 2016; Received in revised form 15 February 2017; Accepted 13 March 2017
Available online 16 March 2017

basis of advanced *in/ex situ* X-ray diffraction (XRD), *ex situ* X-ray photoelectron spectroscopy (XPS) and e*x situ* inductively coupled plasma (ICP) analyses, the $K^+$ pre-intercalation strategy is clearly demonstrated to be an effective way to expand ionic diffusion channels, increase ionic diffusion coefficients, and stabilize interlayer structures, leading to a great improvement in the electrochemical performance. Furthermore, the optimized $K_{0.7}Fe_{0.5}Mn_{0.5}O_2$ exhibits a higher capacity and better cycling stability than $Na_{0.7}Fe_{0.5}Mn_{0.5}O_2$ and $Li_{0.7}Fe_{0.5}Mn_{0.5}O_2$ when investigated as a cathode material for SIBs, indicating that $K_{0.7}Fe_{0.5}Mn_{0.5}O_2$ is a promising candidate for high-capacity and long-life SIBs. Additionally, our study highlights that the $K^+$ intercalation strategy is effective for improving the electrochemical properties of cathode materials for SIBs.

## 2. Experimental section

### 2.1. Synthesis of $K_{0.7}Fe_{0.5}Mn_{0.5}O_2$, $Na_{0.7}Fe_{0.5}Mn_{0.5}O_2$ and $Li_{0.7}Fe_{0.5}Mn_{0.5}O_2$

First, $KNO_3$ (7.0 mmol), $Fe(NO_3)_3{\cdot}9H_2O$ (5.0 mmol), $Mn(CH_3COO)_2$ (5.0 mmol) and $H_2C_2O_4{\cdot}2H_2O$ (4.0 g) were dispersed in deionized water (20 mL) under vigorous stirring at 25 °C to obtain a brownish-red solution. Second, this solution was dried at 60 °C, and baked at 180 °C for 24 h to obtain a loose sponge-like solid. Finally, the sponge-like solid was pre-sintered in air at 500 °C for 2 h and then sintered under argon at 600, 800 and 1000 °C for 10 h (5 °C $min^{-1}$) to obtain $K_{0.7}Fe_{0.5}Mn_{0.5}O_2$. As control experiments, the $K_xFe_{0.5}Mn_{0.5}O_2$ ($0.07 \le x \le 0.56$), $Na_xFe_{0.5}Mn_{0.5}O_2$ ($0.07 \le x \le 0.7$) and $Li_xFe_{0.5}Mn_{0.5}O_2$ ($0.07 \le x \le 0.7$) were synthesized using the same processes, with $KNO_3$ (0.7–5.6 mmol), $NaNO_3$ (0.7–7.0 mmol) and $LiNO_3$ (0.7–7.0 mmol), respectively, used as the alkali-metal-ion sources. All of the chemical reagents were of analytical purity and were purchased from Sinopharm Chemical Reagent Co., Ltd.

### 2.2. Material characterization

*In situ* X-ray diffraction experiments during electrochemical testing of batteries were performed on a D8 Discover X-ray diffractometer equipped with a non-monochromated Co Kα X-ray source; samples were scanned over the 2θ range from of 23° to 45°. For *in situ* XRD measurements, the electrode was placed immediately behind an X-ray-transparent beryllium window that also served as the current collector. The *in situ* XRD signals were collected using a planar detector in a still mode during the charge/discharge processes; each pattern required 120 s to acquire. Cathodes were obtained with 50% active material, 40% acetylene black and 10% polyvinylidene difluoride (PVDF), with N-methyl-2-pyrrolidone solvent used as the solvent. A 1 M $NaClO_4$ solution in a mixture of ethylene carbon/dimethyl carbonate (1:1 w/w) with 2.0 wt% propylene carbonate (electrolyte additive) was used as the electrolyte, and Whatman glass microfiber filter paper (grade GF/F) was used as the separator. The cathode was then cut into square slices with an area of ~0.49 $cm^2$ and a thickness of ~0.1 mm. The loading mass of the active material was approximately 2.4–2.7 mg $cm^{-2}$.

X-ray diffraction (XRD) measurements were performed to obtain crystallographic information using a Bruker D8 Discover X-ray diffractometer equipped with a non-monochromated Co Kα X-ray source. Field-emission scanning electron microscopy (FESEM) images were collected using a JEOL-7100F microscopy. Energy-dispersive X-ray spectroscopy (EDS) was performed using an Oxford EDS IE250. Transmission electron microscopic (TEM) and high-resolution TEM images were recorded using a JEOL JEM-2100F STEM/EDS microscope. Thermal Gravity Analysis (TGA) was performed on an STA-449C. X-ray photoelectron spectroscopy (XPS) analysis was performed using a VG Multilab 2000. Raman spectra were obtained using a Renishaw INVIA micro-Raman spectroscopy system.

### 2.3. Electrochemical measurements

The electrochemical measurements were carried out by assembling type 2016 coin cells in a glove box filled with pure argon gas; sodium discs were used as both the counter electrode and the reference electrode, 1 M $NaClO_4$ in a mixture of ethylene carbon/dimethyl carbonate (1:1 w/w) with 2.0 wt% propylene carbonate (electrolyte additive) was used as the electrolyte, and a Whatman glass microfiber filter paper (grade GF/F) was used as the separator. The cathodes were prepared with 70% active material, 20% acetylene black, and 10% PVDF (using N-methyl-2-pyrrolidone as solvent). The cathodes were cut into square slices with an area and thickness of ~0.49 $cm^2$ and ~0.1 mm, respectively. The loading of the active material was approximately 3.4–3.8 mg $cm^{-2}$. Galvanostatic charge/discharge tests were performed over the potential range from 1.5 to 4.0 V *vs.* $Na/Na^+$ using a multichannel battery testing system (LAND CT2001A). Cyclic voltammetry (CV) and Electrochemical Impedance Spectroscopy (EIS) were conducted using an electrochemical workstation (CHI600E and Autolab PGSTAT 302N).

## 3. Results and discussion

$K_{0.7}Fe_{0.5}Mn_{0.5}O_2$, $Na_{0.7}Fe_{0.5}Mn_{0.5}O_2$ and $Li_{0.7}Fe_{0.5}Mn_{0.5}O_2$ are synthesized *via* a simple and smart organic-acid-assisted strategy (Fig. 1A) [53]. XRD patterns of the three samples which sintered at 800 °C clearly display high crystalline phases (Fig. 1B), however, the samples pre-sintered at 500 °C do not exhibit the characteristics of a layered structure (Fig. S1). All diffraction peaks of the three samples are indexed to a hexagonal lattice with the space group of *P*63/*mmc*, which are iso-structural with P2-type $Na_xCoO_2$ [13–16]. In addition, the XRD pattern of $K_{0.7}Fe_{0.5}Mn_{0.5}O_2$ resemble those of $Na_{0.7}Fe_{0.5}Mn_{0.5}O_2$ and $Li_{0.7}Fe_{0.5}Mn_{0.5}O_2$, suggesting a similar structure. The shift of the diffraction peaks to lower angles is ascribed to the larger potassium ions compared to sodium and lithium ions. Moreover, the 2$\theta$ values of the (002) plane for the three samples are 14.8°, 18.4°, and 21.8° respectively [59,60]. The *d*-spacing of $K_{0.7}Fe_{0.5}Mn_{0.5}O_2$ is 6.94 Å, which is 1.24 times of that of $Na_{0.7}Fe_{0.5}Mn_{0.5}O_2$ (5.58 Å) and 1.47 times of that of $Li_{0.7}Fe_{0.5}Mn_{0.5}O_2$ (4.73 Å), confirming the expanded ion diffusion channel (Fig. S2). Additionally, the XRD patterns of $K_xFe_{0.5}Mn_{0.5}O_2$, $Na_xFe_{0.5}Mn_{0.5}O_2$ and $Li_xFe_{0.5}Mn_{0.5}O_2$ ($0.07 \le x \le 0.7$) are shown in Figs. S3–5. The inductively coupled plasma (ICP) results of $K_{0.7}Fe_{0.5}Mn_{0.5}O_2$, $Na_{0.7}Fe_{0.5}Mn_{0.5}O_2$ and $Li_{0.7}Fe_{0.5}Mn_{0.5}O_2$ are presented in Table S1.

SEM results show that the three samples have similar morphologies that exhibit a slight aggregation (Fig. 1C, E, G). In addition, the particle size of $K_{0.7}Fe_{0.5}Mn_{0.5}O_2$ sintered at 800 °C is more uniform than that of $K_{0.7}Fe_{0.5}Mn_{0.5}O_2$ prepared at 600 °C or 1000 °C (Fig. S6). EDS images show that K, Na (Li shows no signal under the elemental mapping system), Fe and Mn elements (Fig. 1D, F, H) are uniformly distributed on each sample. TEM is used to elucidate the detailed structure of the three samples. The diameters of the individual nanoparticles of $K_{0.7}Fe_{0.5}Mn_{0.5}O_2$ are in the 400–1000 nm range (Fig. 2A, B), whereas those of the $Na_{0.7}Fe_{0.5}Mn_{0.5}O_2$ (Fig. 2F, G) and $Li_{0.7}Fe_{0.5}Mn_{0.5}O_2$ (Fig. 2K, L) are in the 300–900 nm and 100–700 nm ranges, respectively. Carbon layers with thicknesses of ~5 nm (Fig. 2C), ~13 nm (Fig. 2H) and ~2 nm (Fig. 2M) are observed on the surfaces of the $K_{0.7}Fe_{0.5}Mn_{0.5}O_2$, $Na_{0.7}Fe_{0.5}Mn_{0.5}O_2$ and $Li_{0.7}Fe_{0.5}Mn_{0.5}O_2$ nanoparticles, respectively. High-resolution TEM images show that the lattice fringes of $K_{0.7}Fe_{0.5}Mn_{0.5}O_2$, $Na_{0.7}Fe_{0.5}Mn_{0.5}O_2$ and $Li_{0.7}Fe_{0.5}Mn_{0.5}O_2$ are ~0.54 nm (Fig. 2D and inset of Fig. 2D), ~0.45 nm (Fig. 2I and inset of Fig. 2I) and ~0.18 nm (Fig. 2N and inset of Fig. 2N), respectively. The single-crystalline nature of these three samples is demonstrated by their selected-area electron diffraction (SAED) patterns (Fig. 2E, J, and O). Thermogravimetric analysis (TGA) and Raman spectroscopy curves of $K_{0.7}Fe_{0.5}Mn_{0.5}O_2$, $Na_{0.7}Fe_{0.5}Mn_{0.5}O_2$ and $Li_{0.7}Fe_{0.5}Mn_{0.5}O_2$ are shown in Fig. S7.

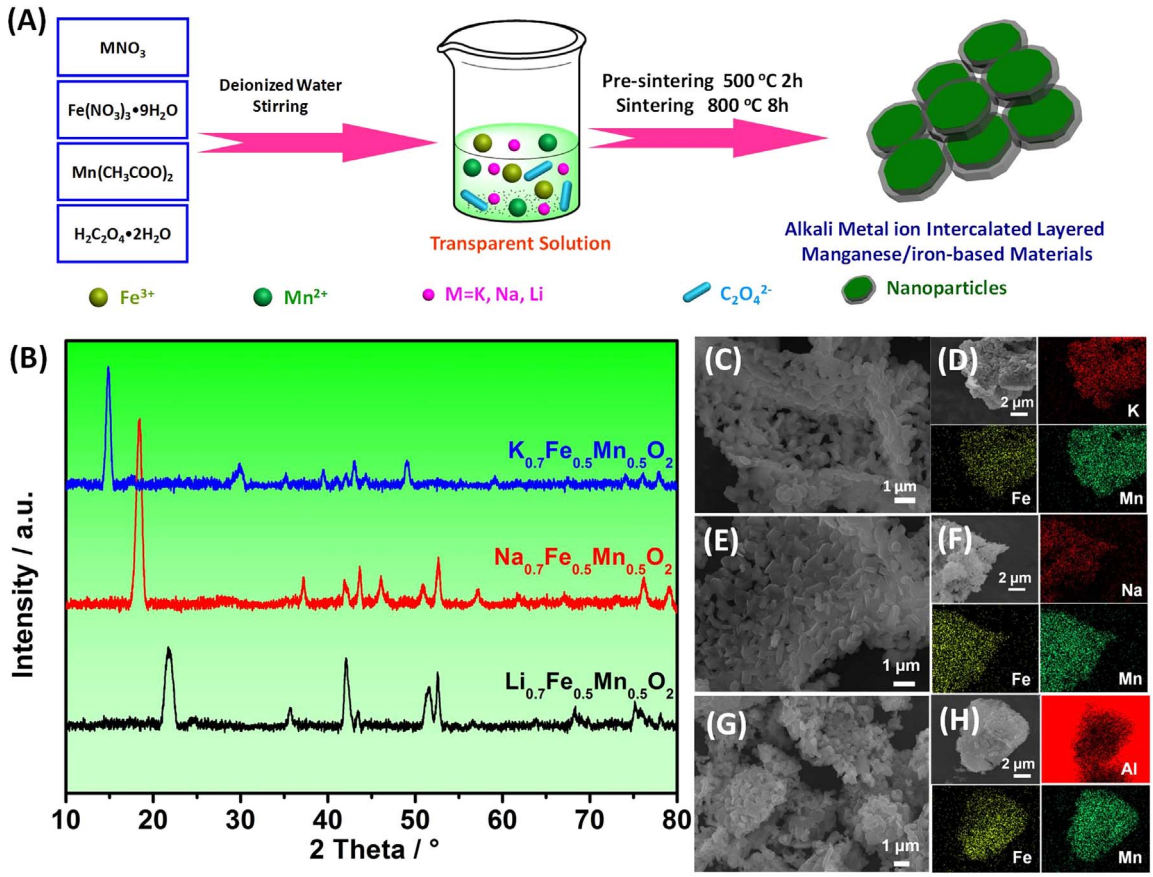


**Fig. 1.** (A) Schematic illustration of the fabrication process for $K_{0.7}Fe_{0.5}Mn_{0.5}O_2$, $Na_{0.7}Fe_{0.5}Mn_{0.5}O_2$ and $Li_{0.7}Fe_{0.5}Mn_{0.5}O_2$. (B) XRD patterns of $K_{0.7}Fe_{0.5}Mn_{0.5}O_2$, $Na_{0.7}Fe_{0.5}Mn_{0.5}O_2$ and $Li_{0.7}Fe_{0.5}Mn_{0.5}O_2$. SEM image (C) and EDS mapping images (D) of $K_{0.7}Fe_{0.5}Mn_{0.5}O_2$. SEM image (E) and EDS mapping images (F) of $Na_{0.7}Fe_{0.5}Mn_{0.5}O_2$. SEM image (G) and EDS mapping images (H) of $Li_{0.7}Fe_{0.5}Mn_{0.5}O_2$.

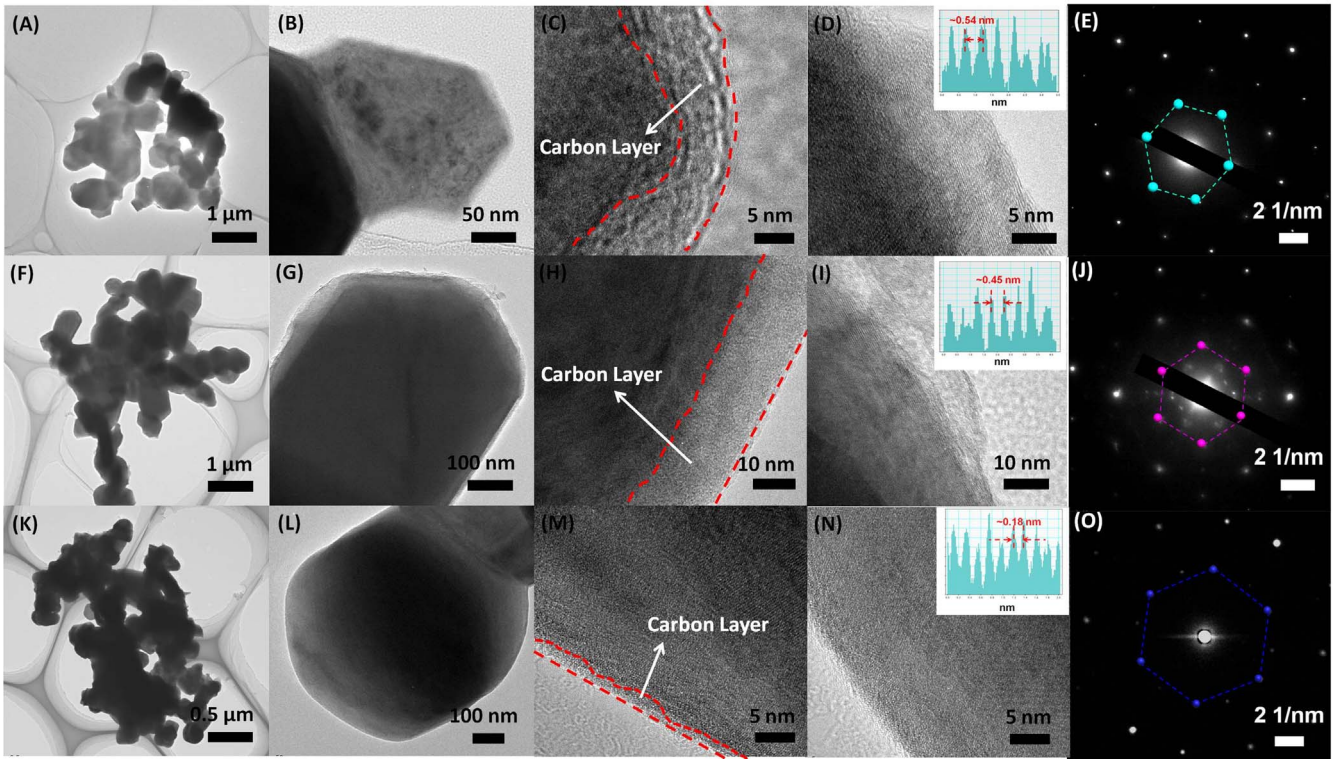


**Fig. 2.** (A-E) TEM images (A, B), high-resolution TEM images (C, D) and SAED pattern (E) of $K_{0.7}Fe_{0.5}Mn_{0.5}O_2$. (F-J) TEM images (F, G), high-resolution TEM images (H, I), and SAED pattern (J) of $Na_{0.7}Fe_{0.5}Mn_{0.5}O_2$. (K-O) TEM images (K, L), high-resolution TEM images (M, N), and SAED pattern (O) of $Li_{0.7}Fe_{0.5}Mn_{0.5}O_2$. Insets of (D), (I) and (N) are the interplanar crystal spacing statistical tables for $K_{0.7}Fe_{0.5}Mn_{0.5}O_2$, $Na_{0.7}Fe_{0.5}Mn_{0.5}O_2$ and $Li_{0.7}Fe_{0.5}Mn_{0.5}O_2$, respectively.

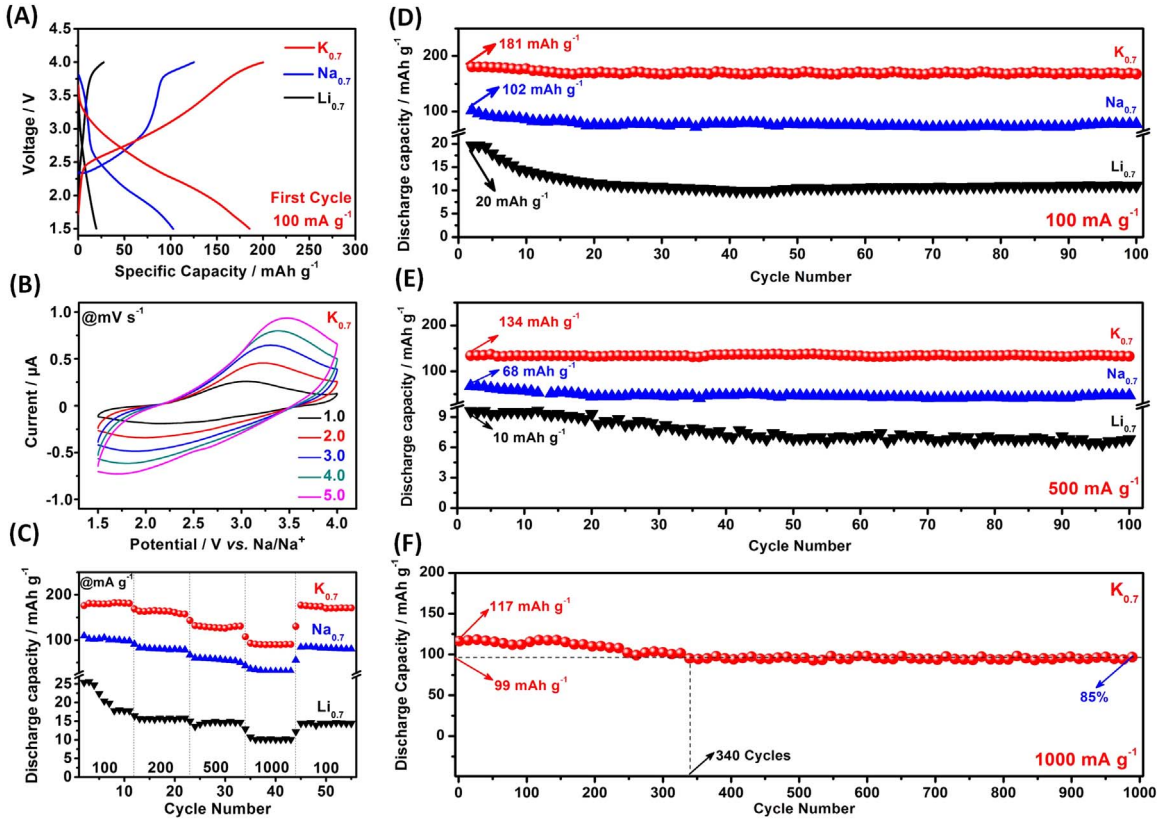


**Fig. 3.** Electrochemical performance of $K_{0.7}Fe_{0.5}Mn_{0.5}O_2$ (denoted as $K_{0.7}$), $Na_{0.7}Fe_{0.5}Mn_{0.5}O_2$ (denoted as $Na_{0.7}$) and $Li_{0.7}Fe_{0.5}Mn_{0.5}O_2$ (denoted as $Li_{0.7}$). (A) Charge/discharge curves. (B) Cyclic voltammograms of $K_{0.7}Fe_{0.5}Mn_{0.5}O_2$ at different scan rates in the electrochemical window from 1.5 to 4.0 V *vs.* $Na/Na^+$. (C) Rate performance of these three cathode materials at various rates ranging from 100 to 1000 and back to 100 mA $g^{-1}$. Cycling measurements for the three cathodes tested at 100 (D) and 500 (E) mA $g^{-1}$. (F) Long-term cycling performance.

The synthesized $K_{0.7}Fe_{0.5}Mn_{0.5}O_2$, $Na_{0.7}Fe_{0.5}Mn_{0.5}O_2$ and $Li_{0.7}Fe_{0.5}Mn_{0.5}O_2$ are tested as cathodes in SIBs. In the case of the $K_{0.7}Fe_{0.5}Mn_{0.5}O_2$ samples, the sample sintered at 800 °C exhibits the best sodium storage performance (Fig. S8). Therefore, 800 °C is considered as the optimized sintering condition. The charge/discharge curves of $K_{0.7}Fe_{0.5}Mn_{0.5}O_2$ show that no obvious plateau appears during the charge and discharge processes (Fig. 3A). However, $Na_{0.7}Fe_{0.5}Mn_{0.5}O_2$ exhibits a pair of weak plateaus (near 3.82 and 1.94 V), and $Li_{0.7}Fe_{0.5}Mn_{0.5}O_2$ exhibits poor charge and discharge characteristics. The CV curves for $K_{0.7}Fe_{0.5}Mn_{0.5}O_2$ (Fig. 3B) show a large hysteresis loop and no obvious cathodic/anodic peaks at different scan rates, unlike the results of $Na_{0.7}Fe_{0.5}Mn_{0.5}O_2$ and $Li_{0.7}Fe_{0.5}Mn_{0.5}O_2$ (Fig. S9). The Coulombic efficiency of the three samples is presented in Fig. S10. The first charge capacity can achieve ~220 mAh $g^{-1}$, corresponding to the extraction of 1.18 $Na^+/K^+$ per formula unit. We observe that 1.18 $Na^+/K^+$ is extracted even though $K_{0.7}Fe_{0.5}Mn_{0.5}O_2$ contains only 0.7 $K^+$. To explain this discrepancy, *ex situ* ICP measurements were conducted. The *ex situ* ICP results show that ~0.41 $Na^+$ are pre-intercalated from the electrolyte into the $K_{0.7}Fe_{0.5}Mn_{0.5}O_2$ prior to charging (Table S2). During the charge process, ~0.41 $Na^+$ and ~0.6 $K^+$ are extracted from the pre-sodiated $K_{0.7}Fe_{0.5}Mn_{0.5}O_2$. After 50 and 100 cycles, the number of $Na^+$ involved in this electrochemical reaction remains stable at ~0.98. To elucidate the reaction mechanism of $K_{0.7}Fe_{0.5}Mn_{0.5}O_2$, we carried out *ex situ* XPS measurements to examine the changes in the oxidation states of Fe and Mn at different charge/discharge states (Fig. S11).

When tested at various current densities in rate measurements, $K_{0.7}Fe_{0.5}Mn_{0.5}O_2$ exhibits a higher initial discharge capacity (182 mAh $g^{-1}$) and better rate recovery (~98%) than those of $Na_{0.7}Fe_{0.5}Mn_{0.5}O_2$ (102 mAh $g^{-1}$, 85%) and $Li_{0.7}Fe_{0.5}Mn_{0.5}O_2$ (21 mAh $g^{-1}$, 80.8%), demonstrating the prominent rate performance (Fig. 3C). $K_{0.7}Fe_{0.5}Mn_{0.5}O_2$ delivers a high initial discharge capacity of 181 mAh $g^{-1}$at 100 mA $g^{-1}$ (Fig. 3D), which is substantially higher than those of $Na_{0.7}Fe_{0.5}Mn_{0.5}O_2$ (102 mAh $g^{-1}$) and $Li_{0.7}Fe_{0.5}Mn_{0.5}O_2$ (20 mAh $g^{-1}$). Notably, the capacity retention of $K_{0.7}Fe_{0.5}Mn_{0.5}O_2$ is as high as 93% (a small capacity decay of 0.07% per cycle) after 100 cycles. By contrast, the $Na_{0.7}Fe_{0.5}Mn_{0.5}O_2$ and $Li_{0.7}Fe_{0.5}Mn_{0.5}O_2$ retain only 76% and 56% of their initial capacities, respectively. When tested at 200 mA $g^{-1}$, $K_{0.7}Fe_{0.5}Mn_{0.5}O_2$ shows the best electrochemical performance compared with $Na_{0.7}Fe_{0.5}Mn_{0.5}O_2$ and $Li_{0.7}Fe_{0.5}Mn_{0.5}O_2$ (Fig. S12).

Remarkably, when measured at 500 mA $g^{-1}$, $K_{0.7}Fe_{0.5}Mn_{0.5}O_2$ exhibits a discharge capacity of 134 mAh $g^{-1}$. Moreover, 96% of the initial discharge capacity is retained after 100 cycles, corresponding to a small capacity fade of 0.01% per cycle. By contrast, the capacity retentions of $Na_{0.7}Fe_{0.5}Mn_{0.5}O_2$ and $Li_{0.7}Fe_{0.5}Mn_{0.5}O_2$ are only 70% and 71%, respectively (Fig. 3E). Even at the high rate of 1000 mA $g^{-1}$, the $K_{0.7}Fe_{0.5}Mn_{0.5}O_2$ delivers an initial discharge capacity of 117 mAh $g^{-1}$ with 85% of the initial capacity retained after 340 cycles, and it can stably operate for 1000 cycles with a capacity of 99 mAh $g^{-1}$, suggesting the outstanding cycling stability (Fig. 3F). To the best of our knowledge, the $K_{0.7}Fe_{0.5}Mn_{0.5}O_2$ in this work exhibits the best electrochemical performance among layered oxides SIB cathodes in terms of the reversible capacity, cycling stability and rate capability (Table S3). Nyquist plots analysis and $Na^+$ diffusion kinetics results show that $K_{0.7}Fe_{0.5}Mn_{0.5}O_2$ exhibit lowest charge transfer resistances ($R_{ct}$) and highest $Na^+$ diffusion coefficient compared to $Na_{0.7}Fe_{0.5}Mn_{0.5}O_2$ and $Li_{0.7}Fe_{0.5}Mn_{0.5}O_2$ (Fig. S13).

To validate the structural stability of $K_{0.7}Fe_{0.5}Mn_{0.5}O_2$ during the charge/discharge processes, *ex situ* XRD experiments are carried out; the obtained patterns are presented in Fig. 4A-C. For $K_{0.7}Fe_{0.5}Mn_{0.5}O_2$ (Fig. 4A) and $Na_{0.7}Fe_{0.5}Mn_{0.5}O_2$ (Fig. 4B), the (002) diffraction peak

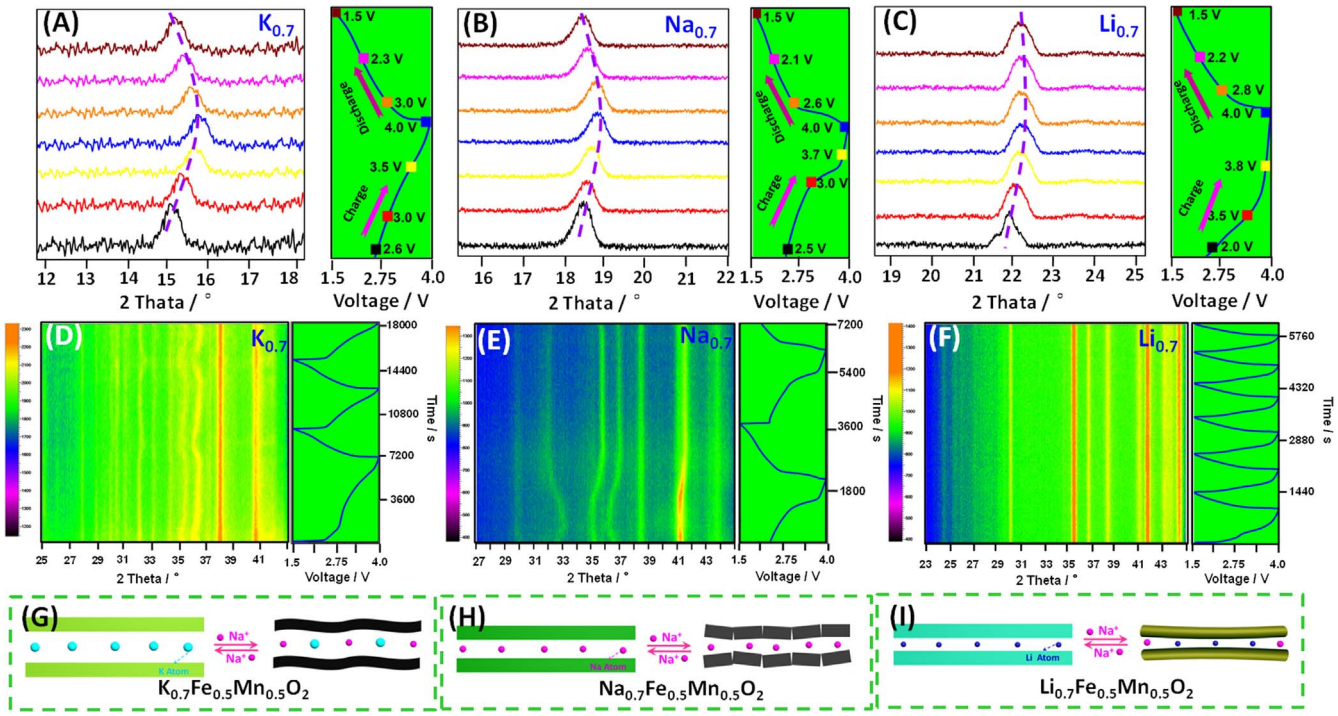


**Fig. 4.** (A-C) *Ex situ* XRD patterns collected at different electrochemical states: the evolution of the (002) diffraction peaks for $K_{0.7}Fe_{0.5}Mn_{0.5}O_2$ (A) and $Na_{0.7}Fe_{0.5}Mn_{0.5}O_2$ (B) during the first cycle at 100 mA $g^{-1}$, respectively, and (C) the evolution of the (002) diffraction peaks of $Li_{0.7}Fe_{0.5}Mn_{0.5}O_2$ during the first cycle at 50 mA $g^{-1}$. (D-F) *In situ* XRD patterns collected during galvanostatic charge/discharge: (D) image plot of the diffraction patterns of $K_{0.7}Fe_{0.5}Mn_{0.5}O_2$ at 25–43° during the charge/discharge cycles at 100 mA $g^{-1}$, (E) image plot of the diffraction patterns of $Na_{0.7}Fe_{0.5}Mn_{0.5}O_2$ at 27–45° during the charge/discharge cycles at 100 mA $g^{-1}$, (F) image plot of the diffraction patterns of $Li_{0.7}Fe_{0.5}Mn_{0.5}O_2$ at 23–45° during the charge/discharge cycles at 50 mA $g^{-1}$. (G-I) Schematic of the sodiation/desodiation processes of $K_{0.7}Fe_{0.5}Mn_{0.5}O_2$, $Na_{0.7}Fe_{0.5}Mn_{0.5}O_2$ and $Li_{0.7}$ $Fe_{0.5}Mn_{0.5}O_2$, respectively.

shifts to higher angles during the charge processes, corresponding to the decrease of the interlamellar *d*-spacing. This trend is reversed during the sodiation processes, corresponding to the insertion of the $K^+$ and $Na^+$, corroborating the high reversibility of the layer structure of both $K_{0.7}Fe_{0.5}Mn_{0.5}O_2$ and $Na_{0.7}Fe_{0.5}Mn_{0.5}O_2$ [53,55,61–63]. For $Li_{0.7}Fe_{0.5}Mn_{0.5}O_2$, the (002) diffraction peak also exhibits slight shift toward higher angles during the charge processes. However, it hardly shifts back to its original site in the subsequent sodiation processes, indicating an irreversible insertion/extraction of ions (Fig. 4C) [64].

To further elucidate the structural evolution during the insertion/de-insertion of $Na^+$, we carried out electrochemical *in situ* XRD experiments; the results are displayed in Fig. 4D-F and Fig. S14. The main peaks of $K_{0.7}Fe_{0.5}Mn_{0.5}O_2$ remain constant throughout the electrochemical processes, except for the gradual shifts of the peak positions and the changes in the peak intensities (Fig. 4D, Fig. S14A). No strong signals of additional peaks associated with other types of structure are observed during the electrochemical cycling, demonstrating that the crystal structure of $K_{0.7}Fe_{0.5}Mn_{0.5}O_2$ is electrochemically stable. However, tiny changes are observed at ~35.0° and ~36.0°, verifying the weak deviation of lattice parameters of the Fe-O or Mn-O octahedra during the charge/discharge processes [44]. Interestingly, the two peaks that shift to high angles during the charge processes can shift back to their original location in the subsequent sodiation processes, demonstrating a highly reversible expansion/contraction of the corresponding lattice distance for the Fe-O or Mn-O octahedra [34]. The slight shift of the position and the intensity variation in the processes of *in situ* test results provide evidence that neither severe phase transition nor a serious structural rearrangement occurs during the ions insertion/extraction process, confirming the highly reversible and stable structure of $K_{0.7}Fe_{0.5}Mn_{0.5}O_2$ (Fig. 4G) [44,55].

However, the $Na_{0.7}Fe_{0.5}Mn_{0.5}O_2$ exhibits a different behavior during the charge/discharge processes. The peaks at ~31.6°, ~35.0°, ~36.5° and ~41.0° clearly change during the first cycle (Fig. 4E, Fig. S14B), showing that the Fe-O or Mn-O octahedra suffer serious distortion. The diffraction peak at ~31.6° also exhibits a slight shift toward higher angles during the charge processes. However, the peaks at ~35.0°, ~36.5° and ~41.0° shift in the opposite direction. Furthermore, none of the peaks are able to shift back to their original positions in the subsequent discharge processes, indicating that the severe distortion of the Fe-O or Mn-O octahedra is irreversible and leads to poor structural stability (Fig. 4H) relative to that of $K_{0.7}Fe_{0.5}Mn_{0.5}O_2$. In the case of $Li_{0.7}Fe_{0.5}Mn_{0.5}O_2$, the *in situ* XRD patterns show that no peaks fluctuate or change in the first cycle or subsequent cycles (Fig. 4F, Fig. S14A). This behavior is attributed to the fact that $Na^+$ can hardly insert into the small interlamellar space of $Li_{0.7}Fe_{0.5}Mn_{0.5}O_2$ (0.98 Å). A few $Na^+$ may insert into the edge of the layer structure or may be adsorbed onto the material surface (Fig. 4I), but these processes do not lead to structural changes during the sodiation/desodiation processes.

To clearly present the effects of three different alkali-metal ions in layered iron/manganese-based materials, we summarize the electrochemical, *ex situ* and *in situ* results as follows: Firstly, the *ex situ* XRD results show that the (002) plane of $K_{0.7}Fe_{0.5}Mn_{0.5}O_2$ shifts to the higher angles with increasing charge voltage and nearly returns to its initial position with the decreasing discharge voltage (Fig. 5A, red symbols), corresponding to the opposite tendency of d-spacing (Fig. 5A, blue symbols). Secondly, the $Na_{0.7}Fe_{0.5}Mn_{0.5}O_2$ exhibits a similar change behaviors; its (002) plane shifts to the higher angles with increasing charge voltage and also returns to its initial position with decreasing charge voltage (Fig. 5B, red symbols), corresponding to the tendency opposite that of the *d*-spacing (Fig. 5B, blue symbols). The reversibility of the *d*-spacing of $Na_{0.7}Fe_{0.5}Mn_{0.5}O_2$ is clearly superior to that of $K_{0.7}Fe_{0.5}Mn_{0.5}O_2$, which is attributed to the difference in the ionic sizes of two species ($K^+ > Na^+$). Finally, the (002) plane of $Li_{0.7}Fe_{0.5}Mn_{0.5}O_2$ shifts to a higher angle with increasing charge voltage (Fig. 5C, red symbols), corresponding to a *d*-spacing decrease (Fig. 5C, blue symbols). However, the (002) plane and *d*-spacing cannot return to their initial positions and instead remain

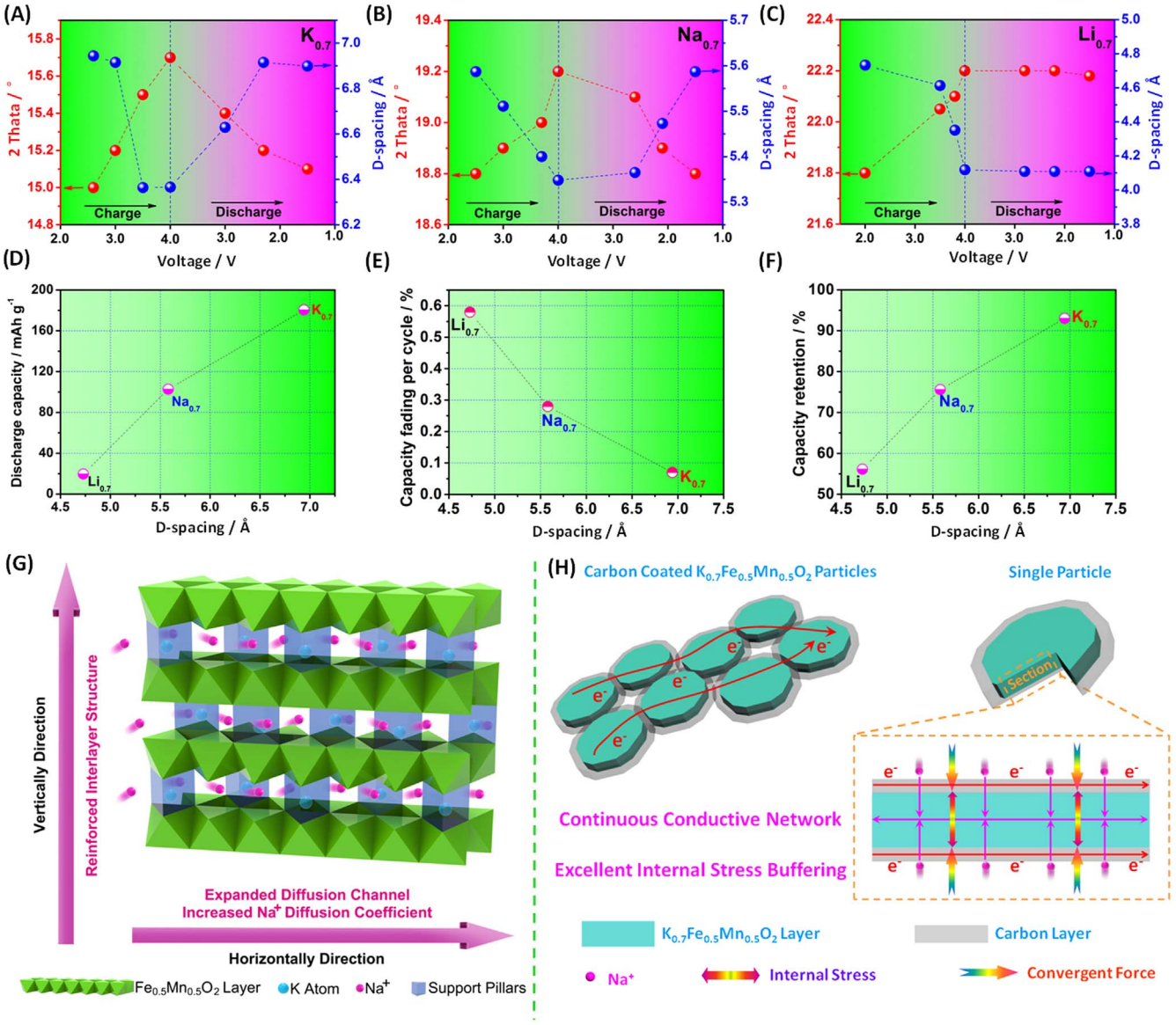


**Fig. 5.** (A-C) Voltage *vs.* (002) peak locations and corresponding *d*-spacings of $K_{0.7}Fe_{0.5}Mn_{0.5}O_2$, $Na_{0.7}Fe_{0.5}Mn_{0.5}O_2$ and $Li_{0.7}Fe_{0.5}Mn_{0.5}O_2$, respectively. Discharge capacity (D), capacity retention (E) and capacity fading per cycle (F) *vs.* the *d*-spacing for $K_{0.7}Fe_{0.5}Mn_{0.5}O_2$, $Na_{0.7}Fe_{0.5}Mn_{0.5}O_2$ and $Li_{0.7}Fe_{0.5}Mn_{0.5}O_2$ at a current density of 100 mA $g^{-1}$. (G) Schematic illustration of the $K_{0.7}Fe_{0.5}Mn_{0.5}O_2$ crystal structure with an enlarged diffusion channel, an increased $Na^+$ diffusion coefficient and a reinforced interlayer structure. (H) Schematic illustration of carbon-coated $K_{0.7}Fe_{0.5}Mn_{0.5}O_2$ particles with a continuous conductive network and excellent internal stress buffering.

unchanged during the discharge processes. Their discharge capacities and capacity retentions increase with increasing interlamellar spacing increase (Fig. 5E-F).

## 4. Conclusions

In conclusion, $K_{0.7}Fe_{0.5}Mn_{0.5}O_2$ nanoparticles are constructed by a simple and smart organic-acid-assisted method. On the basis of *in situ* and *ex situ* XRD characterizations, we confirm that $K_{0.7}Fe_{0.5}Mn_{0.5}O_2$ can provide highly reversible layer spacing variations and an ultra-stable skeleton structure during the charge/discharge processes. Meanwhile, the $K^+$ can act as interlayer pillars, effectively protecting the layered structure from collapse in the vertical direction (Fig. 5G). Moreover, the surface carbon layer can effectively buffer the internal stress, leading to the attractive morphological structure stability (Fig. 5H). In addition, analysis of the diffusion kinetics reveals that large-sized $K^+$ in the interlayer also expands the interlayer structure, leading to a greatly increased $Na^+$ diffusion coefficient in the horizontal direction. As a consequence, when tested as a cathode material for SIBs, the $K_{0.7}Fe_{0.5}Mn_{0.5}O_2$ exhibits superior electrochemical performance in terms of high-capacity and ultra-high cycling stability. Therefore, our study highlights that designing layered oxides with stable structures is a promising strategy to achieve both high energy density and long-term stability for SIB cathode materials.

## Acknowledgements

This work was supported by the National Key Research and Development Program of China (2016YFA0202603), the National Basic Research Program of China (2013CB934103), the Programme of Introducing Talents of Discipline to Universities (B17034), the National Natural Science Foundation of China (51521001, 51602239, 21673171, 51502226), the National Natural Science Fund for Distinguished Young Scholars (51425204), the Hubei Provincial Natural Science Foundation of China (2016CFB267), the China Postdoctoral Science Foundation (2016M592401), and the Fundamental Research Funds for the Central Universities (WUT: 2016III001, 2016III002, 2016III003, 2016IVA090). We thank the

Center for Materials Research and Analysis from Wuhan University of Technology. Prof. Liqiang Mai gratefully acknowledged financial support from China Scholarship Council (No. 201606955096).

## Appendix A. Supplementary material

Supplementary data associated with this article can be found in the online version at doi:10.1016/j.nanoen.2017.03.026.

## References


[1] Z.G. Yang, J.L. Zhang, M.C.W. Kintner-Meyer, X.C. Lu, D. Choi, J.P. Lemmon, J. Liu, Chem. Rev. 111 (2011) 3577–3613.
[2] B. Dunn, H. Kamath, J.M. Tarascon, Science 334 (2011) 928–935.
[3] M. Armand, J.M. Tarascon, Nature 451 (2008) 652–657.
[4] J.W. Choi, D. Aurbach, Nat. Rev. Mater. 1 (2016) 16013.
[5] V. Palomares, P. Serras, I. Villaluenga, K.B. Hueso, J.C. González, T. Rojo, Energy Environ. Sci. 5 (2012) 5884–5901.
[6] H.L. Pan, Y.S. Hu, L.Q. Chen, Energy Environ. Sci. 6 (2013) 2338–2360.
[7] M.D. Slater, D. Kim, E. Lee, C.S. Johnson, Adv. Funct. Mater. 23 (2013) 947–958.
[8] J. Peters, D. Buchholz, S. Passerini, M. Weil, Energy Environ. Sci. 9 (2016) 1744–1751.
[9] D. Kundu, E. Talaie, V. Duffort, L.F. Nazar, Angew. Chem. Int. Ed. 54 (2015) 3431–3448.
[10] E. Talaie, V. Duffort, H.L. Smith, B. Fultz, L.F. Nazar, Energy Environ. Sci. 8 (2015) 2512–2523.
[11] N. Yabuuchi, K. Kubota, M. Dahbi, S. Komaba, Chem. Rev. 114 (2014) 11636–11682.
[12] H. Dong, Y.F. Li, Y.L. Liang, G.S. Li, C.J. Sun, Y. Ren, Y.H. Lu, Y. Yao, Chem. Commun. 52 (2016) 8263–8266.
[13] R. Berthelot, D. Carlier, C. Delmas, Nat. Mater. 10 (2011) 74–80.
[14] M. D'Arienzo, R. Ruffo, R. Scotti, F. Morazzoni, C.M. Mari, S. Polizzi, Phys. Chem. Chem. Phys. 14 (2012) 5945–5952.
[15] R.E. Schaak, T. Klimczuk, M.L. Foo, R.J. Cava, Nature 424 (2003) 527–529.
[16] I.I. Mazin, M.D. Johannes, Nat. Phys. 1 (2005) 91–93.
[17] W. Olszewski, M.Á. Pérez, C. Marini, E. Paris, X.F. Wang, T. Iwao, M. Okubo, A. Yamada, T. Mizokawa, N.L. Saini, J. Phys. Chem. C 120 (2016) 4227–4232.
[18] D. Baster, W. Maziarz, K. Świerczek, A. Stokłosa, J. Molenda, J. Solid State Electrochem. 19 (2015) 3605–3612.
[19] T. Shibata, W. Kobayashi, Y. Moritomo, Appl. Phys. Express 8 (2015) 029201.
[20] S. Komaba, N. Yabuuchi, T. Nakayama, A. Ogata, T. Ishikawa, I. Nakai, Inorg. Chem. 51 (2012) 6211–6220.
[21] M.H. Han, E. Gonzalo, M.C. Cabanas, T. Rojo, J. Power Sources 258 (2014) 266–271.
[22] D. Kim, E. Lee, M. Slater, W.Q. Lu, S. Rood, C.S. Johnson, Electrochem. Commun. 18 (2012) 66–69.
[23] R.Z. Yu, X.Y. Wang, Y.Q. Fu, L.W. Wang, S.Y. Cai, M.H. Liu, B. Lu, G. Wang, D. Wang, Q.F. Ren, X.K. Yang, J. Mater. Chem. A 4 (2016) 4941–4951.
[24] D. Hamania, M. Ati, J.M. Tarascon, P. Rozier, Electrochem. Commun. 13 (2011) 938–941.
[25] M. Guignard, C. Didier, J. Darriet, P. Bordet, E. Elkaïm, C. Delmas, Nat. Mater. 12 (2013) 74–80.
[26] C. Didier, M. Guignard, M.R. Suchomel, D. Carlier, J. Darriet, C. Delmas, Chem. Mater. 28 (2016) 1462–1471.
[27] M. Onoda, J. Phys.-Condens. Mater. 20 (2008) 145205.
[28] N. Yabuuchi, H. Yoshida, S. Komaba, Electrochemistry 80 (2012) 716–719.
[29] X.F. Wang, G.D. Liu, T. Iwao, M. Okubo, A. Yamada, J. Phys. Chem. C 118 (2014) 2970–2976.
[30] S. Kalluri, K.H. Seng, W.K. Pang, Z.P. Guo, Z.X. Chen, H.K. Liu, S.X. Dou, ACS Appl. Mater. Interfaces 6 (2014) 8953–8958.
[31] S.Y. Xu, Y.S. Wang, L.B. Ben, Y.C. Lyu, N.N. Song, Z.Z. Yang, Y.M. Li, L.Q. Mu, H.T. Yang, L. Gu, Y.S. Hu, H. Li, Z.H. Cheng, L.Q. Chen, X.J. Huang, Adv. Energy Mater. 5 (2015) 1501156.
[32] J.M. De Iiaeduya, L. Otaegui, J.M.L. Del Amo, M. Armand, G. Singh, J. Power Sources 337 (2017) 197–203.
[33] Y. Wang, R. Xiao, Y.S. Hu, M. Avdeev, L.Q. Chen, Nat. Commun. 6 (2015) 6954.
[34] C.Y. Yu, J.S. Park, H.G. Jung, K.Y. Chung, D. Aurbach, Y.K. Sun, S.T. Myung, Energy Environ. Sci. 8 (2015) 2019–2026.
[35] H. Kim, D.J. Kim, D.H. Seo, M.S. Yeom, K. Kang, D.K. Kim, Y. Jung, Chem. Mater. 24 (2012) 1205–1211.
[36] M. Yoncheva, R. Stoyanova, E. Zhecheva, E. Kuzmanova, M.S. Vassileva, D. Nihtianova, D. Carlier, M. Guignard, C. Delmas, J. Mater. Chem. 22 (2012) 23418–23427.
[37] D.D. Yuan, W. He, F. Pei, F.Y. Wu, Y. Wu, J.F. Qian, Y.Y. Cao, X.P. Ai, H.X. Yang, J. Mater. Chem. A 1 (2013) 3895–3899.
[38] M.H. Han, E. Gonzalo, N. Sharma, J.M.L.D. Amo, M. Armand, M. Avdeev, J.J.S. Garitaonandia, T. Rojo, Chem. Mater. 28 (2016) 106–116.
[39] X.J. Zhang, G.S. Wang, W.Q. Cao, Y.Z. Wei, J.F. Liang, L. Guo, F. Wu, ACS Appl. Mater. Interfaces 8 (2014) 7471–7478.
[40] V. Duffort, E. Talaie, R. Black, F.N. Linda, Chem. Mater. 27 (2015) 2515–2524.
[41] I. Hasa, D. Buchholz, S. Passerini, J. Hassoun, ACS Appl. Mater. Interfaces 7 (2015) 5206–5212.
[42] Y. Zhou, X.H. Wu, W.W. Wu, K.T. Wang, Ceram. Int. 40 (2014) 13679–13682.
[43] J.S. Thorne, R.A. Dunlap, M.N. Obrovac, J. Electrochem. Soc. 160 (2013) A361–A367.
[44] N. Yabuuchi, M. Kajiyama, J. Iwatate, H. Nishikawa, S. Hitomi, R. Okuyama, R. Usui, Y. Yamada, S. Komaba, Nat. Mater. 11 (2012) 512–517.
[45] C.J. Niu, J.S. Meng, X.P. Wang, C.H. Han, M.Y. Yan, K.N. Zhao, X.M. Xu, W.H. Ren, Y.L. Zhao, L. Xu, Q.J. Zhang, D.Y. Zhao, L.Q. Mai, Nat. Commun. 6 (2015) 7402.
[46] X.F. Wang, M. Tamaru, M. Okubo, A. Yamada, J. Phys. Chem. C 117 (2013) 15545–15551.
[47] E. Gonzalo, M.H. Han, J.M.L.D. Amo, B. Acebedo, M.C. Cabanas, T. Rojo, J. Mater. Chem. A 2 (2014) 18523–18530.
[48] S.M. Oh, S.T. Myung, C.S. Yoon, J. Lu, J. Hassoun, B. Scrosati, K. Amine, Y.K. Sun, Nano Lett. 14 (2014) 1620–1626.
[49] S.H. Guo, P. Liu, H.J. Yu, Y.B. Zhu, M.W. Chen, M. Ishida, H.S. Zhou, Angew. Chem. Int. Ed. 127 (2015) 5992–5997.
[50] J.Y. Hwang, S.M. Oh, S.T. Myung, S.T. Myung, K.Y. Chung, L. Belharouak, Y.K. Sun, Nat. Commun. 6 (2015) 6865.
[51] Y.L. Zhao, C.H. Han, J.W. Yang, J. Su, X.M. Xu, S. Li, L. Xu, R.T. Fang, H. Jiang, X.D. Zou, B. Song, L.Q. Mai, Q.J. Zhang, Nano Lett. 15 (2015) 2180–2185.
[52] Y. Liu, Y. Qiao, W.X. Zhang, H.H. Xu, Z. Li, Y. Shen, L.X. Yuan, X.L. Hua, X. Dai, Y.H. Huang, Nano Energy 5 (2014) 97–104.
[53] X.P. Wang, C.J. Niu, J.S. Meng, P. Hu, X.M. Xu, X.J. Wei, L. Zhou, K.N. Zhao, W. Luo, M.Y. Yan, L.Q. Mai, Adv. Energy Mater. 5 (2015) 1500716.
[54] J.S. Meng, Z.A. Liu, C.J. Niu, X.M. Xu, X. Liu, G.B. Zhang, X.P. Wang, M. Huang, Y. Yang, L.Q. Mai, J. Mater. Chem. A 4 (2016) 4893–4899.
[55] S.S. Fedotov, N.R. Khasanova, A.S. Samarin, O.A. Drozhzhin, D. Batuk, O.M. Karakulina, J. Hadermann, A.M. Abakumov, E.V. Antipov, Chem. Mater. 28 (2016) 411–415.
[56] W.W. Xu, Z.Q. Xie, X.D. Cui, K.N. Zhao, L. Zhang, L.Q. Mai, Y. Wang, J. Mater. Chem. A 4 (2016) 3735–3742.
[57] X.P. Wang, X.M. Xu, C.J. Niu, J.S. Meng, M. Huang, X. Liu, Z.A. Liu, L.Q. Mai, Nano Lett. 1 (2017) 544–550.
[58] S. Jing, D.Y. Hyun, Y.L. Liang, Y.F. Li, Y. Yao, Mater. Res. Express 3 (2016) 064001.
[59] G. Brown, G.W. Brindley, Cryst. St. Clay Miner. X-ray Ident. 5, 1980, pp. 305–359.
[60] L.E. Levine, B.C. Larson, W. Yang, M.E. Kassner, J.Z. Tischler, M.A.D. Reyes, R.J. Fields, W.J. Liu, Nat. Mater. 5 (2006) (619-612).
[61] H. Liu, F.C. Strobridge, O.J. Borkiewicz, K.M. Wiaderek, K.W. Chapman, P.J. Chupas, C.P. Grey, Science 344 (2014) 1252817.
[62] A.Q. Pan, H.B. Wu, L. Zhang, X.W. Lou, Energy Environ. Sci. 6 (2013) 1476–1479.
[63] A.Q. Pan, H.B. Wu, L. Yu, X.W. Lou, Angew. Chem. Int. Ed. 52 (2013) 2226–2230.
[64] E. Lee, D.E. Brown, E.E. Alp, Y. Ren, J. Lu, J.J. Woo, C.S. Johnson, Chem. Mater. 27 (2015) 6755–6764.


**Xuanpeng Wang** received his Master degree from Wuhan University of Technology in 2016. He is currently working toward the Ph.D. degree in Wuhan University of Technology and his current research focuses on the energy storage materials and devices.

**Ping Hu** received his Master degree from Wuhan University of Technology in 2016. He is currently working toward the Ph.D. degree in Wuhan University of Technology and his current research focuses on the energy storage materials and devices.

**Chaojiang Niu** received his Ph.D. degree from Wuhan University of Technology since 2016 and the major is Materials Physics and Chemistry. His current research focuses on the nanomaterials for energy storage.

**Jiashen Meng** received his B.S. degree from Wuhan University of Technology in 2015. He is currently working toward the Ph.D. degree in Wuhan University of Technology and his current research focuses on the energy storage materials and devices.

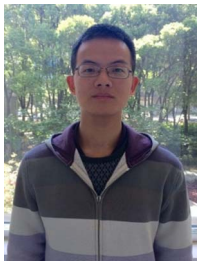

**Xiaoming Xu** received his B.S. degree in Material Science and Engineering from Wuhan University of Technology in 2014. He is currently working toward the Ph.D. degree and his current research focuses on the energy storage materials and devices.

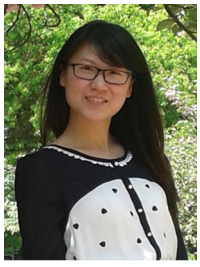

**Xiujuan Wei** received her B.S. degree in Department of Material and Chemical Engineering from Zhengzhou University of Light Industry in 2013. She is working toward the Ph.D. degree in WUT-Harvard Joint Nano Key Laboratory. Her current research involves the transitional metal chalcogenides as anode for lithium ion battery and sodium ion battery.

**Chunjuan Tang** received her Ph.D. degree in Chinese Academy of Sciences in 2008. She has worked in Luoyang Institute of Science and Technology as an associate professor since 2012. Now she is a post doctor in Wuhan University of Technology, whose interests focus on energy storage.

**Wen Luo** received her B.S. degree in Material Science and Engineering from Wuhan University of Technology in 2013. She is currently working toward the Ph.D. degree and his current research focuses on the energy storage materials and devices.

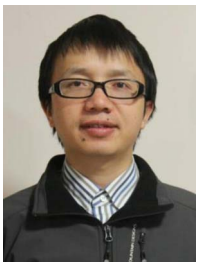

**Liang Zhou** received his Ph.D. (2011) degrees from Department of Chemistry, Fudan University. After graduation, he worked as a postdoctoral research fellow at Nanyang Technological University for 1 year and The University of Queensland for 3 years. He is now a full professor at Wuhan University of Technology and an honorary associate professor at the Australian Institute for Bioengineering and Nanotechnology, The University of Queens-land. His research interests include functional nanomaterials for electrochemical energy storage. Up to now, he has published over 50 papers with a total ISI citation of > 2000 and an h-index of 22.

**Qinyou An** received his Ph.D. degree in Material Science at Wuhan University of Technology. His current research interests include nano energy materials and devices. He is now awful associate professor at Wuhan University of Technology.

**Liqiang Mai** is Chair Professor of Materials Science and Engineering at Wuhan University of Technology (WUT), Distinguished Young Scholar of the National Science Fund of China, Executive Dean of International School of Materials Science and Engineering in WUT. He received Ph.D. degree in WUT in 2004 and then worked as a postdoctoral researcher in Georgia Institute of Technology in the group of Prof. ZL Wang from 2006 to 2007. He conducted nanowire based nano devices and battery research as advanced research scholar in the group of Prof. C. M. Lieber in Harvard University from 2008 to 2011. He is mainly engaged in research field of nano energy materials and micro/nano devices.